Positioning Nuclear Spins in Interacting Clusters for Quantum Technologies and Bio-imaging

Zhen-Yu Wang,* Jan F. Haase,† Jorge Casanova,‡ and Martin B. Plenio§
Institut für Theoretische Physik and IQST, Albert-Einstein-Allee 11, Universität Ulm, D-89069 Ulm, Germany

We propose a method to measure the hyperfine vectors between a nitrogen-vacancy (NV) center and an environment of interacting nuclear spins. Our protocol enables the generation of tunable electron-nuclear coupling Hamiltonians while suppressing unwanted inter-nuclear interactions. In this manner, each nucleus can be addressed and controlled individually thereby permitting the reconstruction of the individual hyperfine vectors. With this ability the 3D-structure of spin ensembles and spins in bio-molecules can be identified without the necessity of varying the direction of applied magnetic fields. We demonstrate examples including the complete reconstruction of an interacting spin cluster in diamond and 3D imaging of all the nuclear spins in a bio-molecule.

arXiv:1510.02811v2 [quant-ph] 11 May 2016

I. INTRODUCTION

Protocols for achieving quantum control and locating the position (positioning) of individual members of nuclear spin ensembles form fundamental building blocks of large scale quantum registers, and may become essential tools for the resolution of the structure and dynamics of individual bio-molecules. The nitrogen-vacancy (NV) center in diamond represents a promising physical platform for the realisation of these protocols even under ambient conditions. This is due to the favourable properties of the electron spin of the NV-center which, in addition to its long coherence times, include the possibility for its optical initialization and read-out together with its coherent manipulation by microwave fields [1–3].

An ensemble of ^{13}C nuclear spins in diamond located in the vicinity of the NV center constitutes an ideal candidate for building a robust quantum memory because of its extremely long coherence times. These nuclear spins can be detected and polarized by the NV center [4–11] and, importantly, NV-^{13}C entangling quantum gates can be implemented [12–14] allowing as an example for the teleportation of quantum information between a nuclear spin and an electron spin in distant diamond samples [15]. Furthermore, NV centers can be implanted close to the diamond surface where they can detect the signal of nuclear spins above the surface with single spin sensitivity [16] which suggests the possibility to examine the structure and dynamics of bio-molecules by means of carefully designed protocols [17–19].

To achieve individual addressing and control of nuclear spins it is necessary to determine the different hyperfine interactions between the NV electron and each nucleus. When inter-nuclear interactions can be neglected, individual nuclear spins with distinct Larmor frequencies can be detected [5–8, 10, 11] and their hyperfine fields can be measured by the variation of the direction of static magnetic fields [7, 17] or with the assumed ability to selectively polarize individual spins [20]. However, in situations involving spin ensembles with similar Larmor frequencies, single spin addressing and complete characterization of hyperfine fields are highly demanding. The situation is even more challenging when the nuclei are closely spaced and interacting between each other via dipolar coupling. In this context, the detection of a single two-spin cluster located at a suitable distance from the NV center and the identification of part of their interactions has been achieved [4, 9]. However, a method to identify each spin in a spin cluster and thereby completely characterize the Hamiltonian of the spin-cluster is, to the best of our knowledge, unknown.

Recently, it has been shown that for distant nuclear spins such that an applied magnetic field can be much stronger than the hyperfine interactions, one can significantly improve the addressing of individual nuclear spins [11]. Such a strong magnetic field is also required when nuclear control fields are applied, e.g., for decoupling of nuclear dipolar interactions, since the nuclear Zeeman energies should be much stronger than the amplitudes of nuclear control fields. Importantly, however, under such magnetic fields the method for reconstructing the hyperfine vector described in [7] is not useful anymore. This is because a magnetic field not oriented along the NV symmetry axis causes a different spin mixing in the NV electron ground and excited states. This destroys the optical qualities damaging, therefore, the initialization and read-out of NV center. Furthermore, it has been experimentally shown that tilting the magnetic field away from the NV axis reduces the collected photoluminescence, and the difference in fluorescence counts could be noticeable even when the angle between the magnetic field and NV axis is as small as 0.1° [21].

In this work, we overcome the difficulties in the measurement of the hyperfine field in spin ensembles and propose a quantum control method for individual spin manipulation and three-dimensional (3D) positioning of spin ensembles. The method combines a robust dynamical decoupling (DD) protocol [11] on NV electron spin with the presence of two radio-frequency (rf) fields acting on the nuclear spins, see Fig. 1. One of the rf fields, the rf decoupling field, is used to eliminate the internuclear interactions while the other one, the rf control field, is responsible for achieving the selective spin manipulation. The measurement of the directions of hyperfine fields is achieved by using the phase of rf control field to break the symmetry of the system Hamiltonian. Remarkably, this protocol is insensitive to amplitude fluctuations in the rf control field.

Without the need for magnetic field reorientation, which is time consuming in current laboratory set-ups and also affects

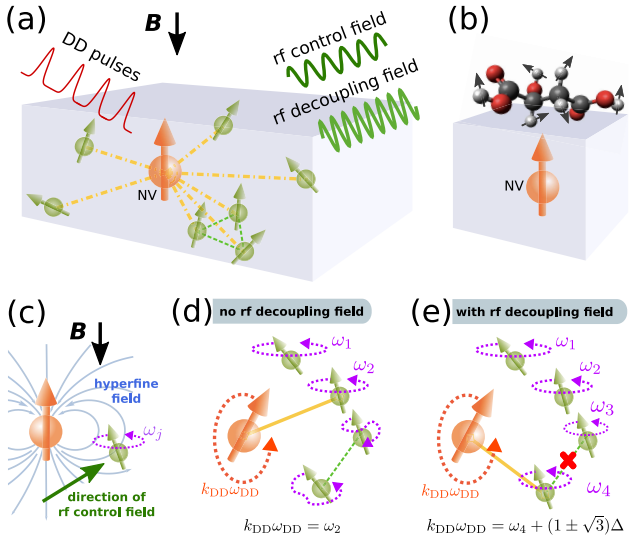

FIG. 1. (color online). Individual 3D positioning and control of nuclear spins with an NV center in diamond, by using rf decoupling and control fields and DD pulse sequences. (a) Our method enables selective addressing and control of a single nuclear spin (denoted by the yellow dashed dotted lines), e.g., in a coupled cluster (with nuclear dipolar coupling highlighted by green dashed lines) thus enabling quantum information processing protocols in quantum registers. (b) Application of the method to structure analysis of a single molecule by 3D positioning of spins which may be coupled by dipolar interactions. (c)-(e) Illustrations of the principles of the scheme for measurement and control. (c) The Larmor frequencies ω_j of nuclear spins are shifted by the position-dependent hyperfine field, which is symmetric about the NV axis. The 3D positions of nuclear spins are measured by the combination of the rf control and the hyperfine field, where the former is used to break the symmetry of the system. (d) When the characteristic flipping frequency of the NV electron spin under DD control matches the Larmor frequency of the target spin, the target spin is addressed through resonant coupling (denoted by yellow solid line). Without rf decoupling field, coupled spins (linked by green dashed lines) do not precess at their Larmor frequencies and can not be individually addressed. (e) The rf decoupling field suppresses the nuclear dipolar interactions and enables individual addressing and control of the spins in the coupled spin cluster.

fluorescence properties of NV centers, our method can implement fast detection, structure analysis, and control of spin ensembles. With the ability to work at strong magnetic fields without changing their directions, good qualities of the optical control on NV electron spin are preserved, and therefore our method has applications in the detection of homonuclear spins with chemical shifts which is relevant for structure determination of bio-molecules.

The paper is organized as follows. In Sec.II we describe the theory that is underlying individual addressing and control of nuclear spins in a nuclear ensemble by an NV center together with the methods to eliminate the internuclear coupling. In Sec.III, schemes to measure the hyperfine interactions and resolving the structure of nuclear spin ensembles are presented with detailed numerical demonstrations, which include 3D positioning of a non-interacting spin ensemble, complete characterization of an interacting ^{13}C spin cluster, and 3D positioning and imaging of all the nuclear spins in a bio-molecule. The conclusions are drawn in Sec.IV.

II. THEORY AND METHOD

A. Microscopic model

The quantum system composed of an NV center electron spin and its nuclear environment is described by the Hamiltonian

$$H = H_{\rm NV}^{\rm GS} + H_{\rm hf} + H_{\rm nZ} + H_{\rm nn}. \quad (1)$$

Here the ground-state NV electron spin Hamiltonian is $H_{\rm NV}^{\rm GS} = D(\boldsymbol{S}\cdot\hat{z})^2 - \gamma_e \boldsymbol{B}\cdot\boldsymbol{S}$, where $\boldsymbol{S} = (S_x, S_y, S_z)$ is a spin-1 operator, the axis of the NV-center is oriented along z-direction with unit vector $\hat{z}$, $\boldsymbol{B}$ denotes an external (static) magnetic field, γ_e is the electron spin gyromagnetic ratio, and the ground state zero field splitting $D = 2\pi \times 2.87$ GHz. The nuclear Zeeman Hamiltonian $H_{\rm nZ} = -\sum_j \gamma_j \boldsymbol{B}\cdot\boldsymbol{I}_j$, where $\boldsymbol{I}_j = (I_j^x, I_j^y, I_j^z)$ and γ_j are the j-th nuclear spin operator and gyromagnetic ratio respectively. Since tilting the magnetic field away from the NV axis will introduce errors in measurements, we fix the magnetic field along the NV symmetry axis $\boldsymbol{B} = B_z\hat{z}$. The electron spin couples to the nuclei via the hyperfine interaction $H_{\rm hf}$, and the nuclear magnetic dipole-dipole interaction $H_{\rm nn}$ reads

$$H_{\rm nn} = \sum_{j>k} \frac{\mu_0}{4\pi}\frac{\gamma_j\gamma_k}{r_{j,k}^3}\left[\boldsymbol{I}_j\cdot\boldsymbol{I}_k - \frac{3(\boldsymbol{I}_j\cdot\boldsymbol{r}_{j,k})(\boldsymbol{r}_{j,k}\cdot\boldsymbol{I}_k)}{r_{j,k}^2}\right], \quad (2)$$

with μ_0 being the vacuum permeability, $\boldsymbol{r}_{j,k} = \boldsymbol{r}_j - \boldsymbol{r}_k$ the difference between the k-th and j-th nuclear positions, and $r_{j,k} = |\boldsymbol{r}_{j,k}|$.

Typically the electron-nuclear flip-flop terms in the hyperfine interaction $H_{\rm hf}$ are suppressed by the large energy splitting (~GHz) between the spin triplet ground states $|0\rangle$ and $|m_s\rangle$ ($m_s = \pm 1$) that exceeds significantly the hyperfine coupling. In this way, we write the Hamiltonian H in the rotating frame of $H_{\rm NV}^{\rm GS}$ and, when restricted to the manifold of two Zeeman sublevels $|0\rangle$ and $|m_s\rangle$, we find

$$H_{0,m_s} = H_{\rm int} + H_{\rm nZ}^{\rm eff} + H_{\rm nn}. \quad (3)$$

Here the hyperfine interaction between the NV electron spin and nuclear spins reads

$$H_{\rm int} = m_s\frac{\sigma_z}{2}\sum_j \boldsymbol{A}_j\cdot\boldsymbol{I}_j, \quad (4)$$

with $\sigma_z = |m_s\rangle\langle m_s| - |0\rangle\langle 0|$ and $\boldsymbol{A}_j$ the hyperfine vectors. The nuclear Zeeman Hamiltonian becomes

$$H_{\rm nZ}^{\rm eff} = -\sum_j \boldsymbol{\omega}_j\cdot\boldsymbol{I}_j, \quad (5)$$

where

$$\boldsymbol{\omega}_j \equiv \omega_j \hat{\omega}_j \equiv \gamma_j B_z \hat{z} - \frac{m_s}{2}\boldsymbol{A}_j, \tag{6}$$

and the Larmor frequency $\omega_j = |\boldsymbol{\omega}_j|$ is shifted by the hyperfine fields $\boldsymbol{A}_j$. It is the hyperfine vector $\boldsymbol{A}_j$ that we wish to measure accurately, which is important in NV center based quantum information processing and sensing.

B. Quantum control

1. Decoupling of nuclear magnetic dipole interactions

Magnetic dipolar coupling between nuclei, $H_{\rm nn}$, interferes with the individual NV center-nucleus entangling processes and creates difficulties for single-spin measurement. To show how to suppress the dipolar coupling $H_{\rm nn}$, we first consider a special case when the Larmor frequencies $\boldsymbol{\omega}_j$ and hence $\omega_j = |\boldsymbol{\omega}_j|$ are equal for the coupled spins. Under a strong magnetic field, the single-spin flipping term in $H_{\rm nn}$ are suppressed, yielding

$$H_{\rm nn} \approx \sum_{j>k} \frac{\mu_0}{8\pi}\frac{\gamma_j\gamma_k}{r_{j,k}^3}\left[1 - \frac{3(\boldsymbol{r}_{j,k}\cdot\hat{z})^2}{r_{j,k}^2}\right]\left(3I_j^z I_k^z - \boldsymbol{I}_j\cdot\boldsymbol{I}_k\right). \tag{7}$$

The interaction $H_{\rm nn}$ given by Eq. (7) can be canceled in a rotating frame where the spins rotate at an angle of $\arccos(1/\sqrt{3})$ (the "magic angle") with respect to $\boldsymbol{B}$ according to the Lee-Goldburg irradiation method [22–24]. This can be achieved by means of rf-driving with a Rabi frequency $\sqrt{2}\Delta$ and a detuning Δ with respect to the nuclear energy ω_j [25]. When the spinning rate determined by Δ exceeds the strength of $H_{\rm nn}$, the internuclear interaction is averaged out.

In the general case, and because of the different values of the hyperfine vectors $\boldsymbol{A}_j$ for different nuclei, the Larmor frequencies $\boldsymbol{\omega}_j$ have distinct values and the quality of the decoupling by magic spinning needs to be reassessed. In Appendix A we show that the dipolar coupling $H_{\rm nn}$ can still be suppressed when the rf decoupling field is strong compared with the differences of $\boldsymbol{\omega}_j$. The basic idea is the following. The rf decoupling field for suppressing $H_{\rm nn}$ reads

$$H_{\rm rfd}(t) = \sum_j \gamma_j V_{\rm rfd}\cos(\omega_{\rm rfd}t - \phi_{\rm rfd})\hat{n}_{\rm rf}\cdot\boldsymbol{I}_j, \tag{8}$$

where the field direction $\hat{n}_{\rm rf}$ may be fixed by a coplanar waveguide on the diamond chip. In the interaction picture of the nuclear Zeeman Hamiltonian $H_{\rm nZ}$, the parallel component $\boldsymbol{n}_j^z = (\hat{n}_{\rm rf}\cdot\hat{\omega}_j)\hat{\omega}_j$ in $H_{\rm rfd}(t)$ is neglected under the rotating wave approximation (RWA) and $H_{\rm rfd}(t)$ drives the spins at the Rabi frequencies $\Omega_j^{\rm rfd} = \frac{1}{2}\gamma_j V_{\rm rfd}|\boldsymbol{n}_j(\phi_{\rm rfd})|$, where the direction of effective rf driving

$$\boldsymbol{n}_j(\phi_{\rm rfd}) \equiv \boldsymbol{n}_j^x\cos\phi_{\rm rfd} + \boldsymbol{n}_j^y\sin\phi_{\rm rfd}, \tag{9}$$

is perpendicular to $\hat{\omega}_j$. Here $\boldsymbol{n}_j^x = \hat{n}_{\rm rf} - \boldsymbol{n}_j^z$ and $\boldsymbol{n}_j^y = \hat{\omega}_j\times\hat{n}_{\rm rf}$. Under a strong magnetic field, $\hat{\omega}_j \approx \hat{z}$ and we choose $\Omega_j^{\rm rfd} \approx \frac{1}{2}\gamma_j V_{\rm rfd}\sqrt{1-|\hat{n}_{\rm rf}\cdot\hat{z}|^2} = \sqrt{2}\Delta$ on the target spins. Other spin species with different values for γ_j are not driven because of the large frequency mismatches under strong magnetic fields. For spins with the same γ_j there is a shift in the detuning Δ given by

$$\delta_j \equiv (\omega_{\rm rfd} - \omega_j) - \Delta, \tag{10}$$

which characterizes the shift in ω_j. Because the nuclear-nuclear interactions decay fast with the distance as $1/r_{j,k}^3$, only closely spaced nuclear spins have non-negligible coupling. Those closely spaced spins have relatively small differences δ_j. When the rf driving is much stronger than δ_j, i.e., $\delta_j \ll \Delta$, the coupled spins are following the same magic spinning to a very good approximation and therefore interactions between them are suppressed either by the magic spinning decoupling or by a reduction factor $\propto \delta_j/\Delta$ (see Appendix A). In this manner, and for the sake of clarity in the presentation, we neglect $H_{\rm nn}$ in the following analytical work but retain it in our numerics.

2. DD control on the NV center

In order to address a single spin, we apply DD pulse sequences, which can be realized by microwave control or optical driving [2, 26]. In this way decoherence caused by slow magnetic fluctuations (e.g., drifts in static magnetic fields caused by temperature fluctuations) can be efficiently suppressed by the DD sequences through the fast averaging of these effects on the spin states [27]. Each of the DD π pulse flips the electron spin states, i.e., $|0\rangle \leftrightarrow |m_s\rangle$, in a time much shorter than the time scale of other system dynamics. Therefore in the following the π pulses are treated as instantaneous. Each π pulse introduces a minus sign on the σ_z operator in $H_{\rm int}$ [Eq. (4)]. That is, the DD pulse sequence leads to the transformation $\sigma_z \to F(t)\sigma_z$, where the modulation function $F(t)$ takes the values $+1$ or -1 depending whether an even or odd number of π pulses have been applied. In this way, under DD control the interaction Hamiltonian reads

$$H_{\rm int}(t) = m_s F(t)\frac{\sigma_z}{2}\sum_j \tilde{\boldsymbol{A}}_j(t)\cdot\boldsymbol{I}_j, \tag{11}$$

in a rotating frame with respect to

$$H_{\rm n}(t) = H_{\rm nZ}^{\rm eff} + H_{\rm rfd}(t), \tag{12}$$

where $H_{\rm nZ}^{\rm eff}$ and $H_{\rm rfd}(t)$ are given by Eqs. (5) and (8) respectively. In Eq. (11) we have $\tilde{\boldsymbol{A}}_j(t)\cdot\boldsymbol{I}_j = U_{\rm n}^\dagger(t)\boldsymbol{A}_j\cdot\boldsymbol{I}_j U_{\rm n}(t)$, where $U_{\rm n}(t) = \mathcal{T}e^{-i\int_0^t H_{\rm n}(\tau)d\tau}$ with $\mathcal{T}$ being the time-ordering operator. We show in Appendix A that

$$\tilde{\boldsymbol{A}}_j(t) = \tilde{\boldsymbol{A}}_j^x(t)\cos(\omega_{\rm rfd}t) + \tilde{\boldsymbol{A}}_j^y(t)\sin(\omega_{\rm rfd}t) + \tilde{\boldsymbol{A}}_j^z(t), \tag{13}$$

$$\tilde{\boldsymbol{A}}_j^\alpha(t) \equiv (\boldsymbol{A}_j^\alpha - \boldsymbol{A}_j^\alpha\cdot\hat{\nu}_j\hat{\nu}_j)\cos(\nu_j t) - \hat{\nu}_j\times\boldsymbol{A}_j^\alpha\sin(\nu_j t) + \boldsymbol{A}_j^\alpha\cdot\hat{\nu}_j\hat{\nu}_j,\ \alpha = x,y,z, \tag{14}$$

$$\boldsymbol{A}_j^x \equiv \boldsymbol{A}_j - \boldsymbol{A}_j^z, \tag{15}$$

$$\boldsymbol{A}_j^y \equiv \hat{\omega}_j \times \boldsymbol{A}_j, \tag{16}$$

$$\boldsymbol{A}_j^z \equiv \boldsymbol{A}_j \cdot \hat{\omega}_j \hat{\omega}_j, \tag{17}$$

under a rf field with $\omega_{\rm rfd} \sim \omega_j \gg \gamma_j V_{\rm rfd}$. Here $\boldsymbol{A}_j^x$ and $\boldsymbol{A}_j^y$ are perpendicular to $\hat{\omega}_j$, and $\hat{\nu}_j$ is the unit vector of

$$\boldsymbol{\nu}_j = \frac{1}{2}\gamma_j V_{\rm rfd} \boldsymbol{n}_j(\phi_{\rm rfd}) + (\omega_{\rm rfd} - \omega_j)\hat{\omega}_j, \tag{18}$$

whose modulus reads $\nu_j = |\boldsymbol{\nu}_j| = \sqrt{(\Omega_j^{\rm rfd})^2 + (\omega_{\rm rfd} - \omega_j)^2}$. Physically, $\tilde{\boldsymbol{A}}_j(t)$ is the vector $\boldsymbol{A}_j$ after two subsequent rotations. The first rotates the vector $\boldsymbol{A}_j$ about the axis $\hat{\omega}_j$ by an angle $\omega_{\rm rfd} t$ while the second one is a rotation around the axis $\hat{\nu}_j$ by an angle $\nu_j t$.

When choosing $\Omega_j^{\rm rfd} = \sqrt{2}\Delta$ for achieving internuclear decoupling, see Appendix A, the amplitude of the spinning rate by rf driving

$$\nu_j = \Delta\sqrt{2 + (1 + \delta_j/\Delta)^2} \approx \sqrt{3}\Delta + \frac{1}{\sqrt{3}}\delta_j, \tag{19}$$

has a strength $\sqrt{3}\Delta$ up to a spin dependent shift. When there is no rf decoupling field $V_{\rm rfd} = \omega_{\rm rfd} = 0$, $\boldsymbol{\nu}_j = -\boldsymbol{\omega}_j$, and Eq. (13) reads $\tilde{\boldsymbol{A}}_j(t) = \boldsymbol{A}_j^x \cos(\omega_j t) + \boldsymbol{A}_j^y \sin(\omega_j t) + \boldsymbol{A}_j^z$, which contains terms that oscillate at the Larmor frequency ω_j. When the rf decoupling field has been applied, $\tilde{\boldsymbol{A}}_j(t)$ contains terms that oscillate at the frequencies ν_j and $\omega_{\rm rfd} \pm \nu_j$ which can be obtained by expanding $\tilde{\boldsymbol{A}}_j(t)$ with the use of product-to-sum trigonometric formulas. In both cases the spin-dependent oscillating harmonics can be utilized to individually address different nuclear spins.

3. *Individual nuclear spin addressing*

For periodic DD pulses, the modulation function $F(t) = F(t + \tau_{\rm DD})$ can be expanded in a Fourier series such that for even $F(t)$ we have

$$F(t) = \sum_{k\geq 1} f_k \cos(k\omega_{\rm DD} t), \tag{20}$$

where $\tau_{\rm DD} = 2\pi/\omega_{\rm DD}$ describes the period of the DD sequence. The lowest frequency in this expansion, i.e., $\omega_{\rm DD}$ characterizes the flipping rate of the NV electron spin by the DD pulses. When $\omega_{\rm DD}$ or its multiples do not match the characteristic frequencies of the surrounding nuclear spin ensemble (the Larmor frequencies ω_j for the case of no rf decoupling field), then the interaction $H_{\rm int}(t)$ (see Eq. (4)) is suppressed. Under DD control we can arbitrarily tune $\omega_{\rm DD}$ and when the DD pulses are tuned to a resonance with the target nuclear spins (e.g., $k_{\rm DD}\omega_{\rm DD} = \omega_j$ for the case of no rf decoupling field) the interaction Hamiltonian in Eq. (11) couples the NV electron and target nuclear spins

In the literature, the most widely used DD sequences for coherence protection and spin detection are the Carr-Purcell-Meiboom-Gill (CPMG) [28, 29] and the XY family [30, 31] sequences of pulses, which have fixed expansion coefficients $f_k = 4(k\pi)^{-1}\sin(\frac{k\pi}{2})$ in Eq. (20). However, recently it was demonstrated that the ability to tune the expansion coefficients f_k can lead to a considerable enhancement in resolution and hence single spin addressing [11, 32–34]. In particular, the adaptive-XY (AXY) sequences in Ref. [11] tune the f_k for highly selective spin addressing while remaining robust against detuning and pulse amplitude errors. Under typical error regimes and for typical control parameters in experiments of DD control on NV centers, simulations show that the AXY sequences behave well even when the number of DD pulses reaches several thousands [11]. In this work we adopt the AXY sequence for its excellent abilities for individual spin addressing and robustness, even though the theory to be described below is general and applies to other DD schemes such as CPMG or any decoupling sequence of the XY family.

When the dipolar coupling $H_{\rm nn}$ is negligible during the time of the protocol, the rf decoupling field $H_{\rm rfd}(t)$ in Eq. (8) is not necessary. If $H_{\rm rfd}(t) = 0$, $\tilde{\boldsymbol{A}}_j(t)$ [Eq. (13)] has components oscillating at the Larmor frequency ω_j. When the frequency of the $k_{\rm DD}$-th harmonic in the expansion Eq. (20) matches the Larmor frequency ω_n of the n-th spin, i.e., the scanning frequency satisfies

$$\omega_{\rm scan} = \omega_n = k_{\rm DD}\omega_{\rm DD}, \tag{21}$$

we have resonant coupling between the NV center and the n-th spin. For a sufficiently strong magnetic field $\gamma_j B_z \sim \omega_j \gg |\boldsymbol{A}_j|$, we have the effective Hamiltonian under RWA [11]

$$H_{\rm int}(t) \approx \frac{m_s}{4} f_{k_{\rm DD}} \sigma_z \boldsymbol{A}_n^x \cdot \boldsymbol{I}_n, \tag{22}$$

whose validity requires that the following conditions are satisfied (with $j \neq n$)

$$|\gamma_j B_z| \gg k_{\rm DD}|\boldsymbol{A}_j|, \tag{23}$$

$$|\omega_n - \omega_j| \gg |f_{k_{\rm DD}} \boldsymbol{A}_j^x|. \tag{24}$$

The first condition, which limits the largest possible $k_{\rm DD}$, can be reached by a strong magnetic field while the second condition can be met by the AXY sequences, which can tune $f_{k_{\rm DD}}$ to arbitrarily small values without the necessity of using high harmonics, i.e., high values of $k_{\rm DD}$. The first condition can also be reached by a sufficiently large distance between the NV center and the nuclear spins, because of the reduction of the hyperfine field $\boldsymbol{A}_j$. It should be noted though that a large distance also imposes difficulties on individual spin addressing because of reduced differences among the hyperfine-field shifted Larmor frequencies ω_j.

If an rf decoupling field has been used to suppress the interaction $H_{\rm nn}$, $\tilde{\boldsymbol{A}}_j(t)$ [Eq. (13)] contains terms that oscillate at the frequencies ν_j and $\omega_{\rm rfd} \pm \nu_j$. When the resonance conditions

$$k_{\rm DD}\omega_{\rm DD} = \nu_n \;\text{ or }\; k_{\rm DD}\omega_{\rm DD} = \omega_{\rm rfd} \pm \nu_n \tag{25}$$

are satisfied, then there is coupling between the NV electron spin and the n-th spin analogous to Eq. (22). The Larmor frequencies ω_n can be detected by scanning simultaneously the

frequencies of rf decoupling field and $\omega_{\rm DD}$ of pulse sequences. For example, we may choose the rf decoupling field with the Rabi driving $\Omega_j^{\rm rfd} = \sqrt{2}\Delta$ and frequency

$$\omega_{\rm rfd} = \omega_{\rm scan} + \Delta, \tag{26}$$

and, at the same time, the DD sequence with

$$k_{\rm DD}\omega_{\rm DD} = \omega_{\rm scan} + (1 \pm \sqrt{3})\Delta. \tag{27}$$

When the scanning frequency $\omega_{\rm scan} = \omega_n$, the resonance condition Eq. (25) is reached with $\delta_n = 0$ [Eq. (10)]. For nearby spins coupled to the n-th spin, δ_j is small, and the rf decoupling field with $\delta_j \ll \Delta$ suppresses the nuclear dipolar coupling to the n-th spin. Similar to the case in obtaining Eq. (22), we can neglect fast oscillating terms under RWA. The effective Hamiltonian for the resonance Eq. (25) reads

$$H_{\rm int}(t) \approx \frac{m_s}{8} f_{k_{\rm DD}} \sigma_z \boldsymbol{a}_n^{\pm} \cdot \boldsymbol{I}_n, \tag{28}$$

$$\boldsymbol{a}_n^{(\pm)} \equiv \boldsymbol{A}_n^x - \boldsymbol{A}_n^x \cdot \hat{\nu}_n \hat{\nu}_n \pm \hat{\nu}_n \times \boldsymbol{A}_n^y, \tag{29}$$

under the conditions Eq. (23),

$$|\gamma_j B_z| \gg \Delta, \tag{30}$$

$$\sqrt{3}\Delta \gg |f_{k_{\rm DD}} \boldsymbol{A}_j|, \tag{31}$$

$$\left||\gamma_j B_z| k/k_{\rm DD} - \sqrt{3}\Delta\right| \gg |\boldsymbol{A}_j|, \forall k \geq 1, \tag{32}$$

and the addressing condition

$$|\nu_j - \nu_n| \gg |f_{k_{\rm DD}} \boldsymbol{A}_j|. \tag{33}$$

The condition Eq. (30) guarantees the validity of rf driving. The condition Eq. (23) eliminates the static terms in $\tilde{\boldsymbol{A}}_j(t)$ because of the fast oscillation in $F(t)$. The time-dependent terms in $\tilde{\boldsymbol{A}}_j(t)$ carry the frequencies $\nu_j \approx \sqrt{3}\Delta$ and $\omega_{\rm rfd} \pm \nu_j \sim |\gamma_j B_z|$ because of Eq. (30), while the function $F(t)$ carries the frequencies $k\omega_{\rm DD} \sim |\gamma_j B_z| k/k_{\rm DD}$. Thus, for $k = k_{\rm DD}$, we need Eq. (31) to eliminate the relevant time-dependent terms, while to eliminate the terms having $k \neq k_{\rm DD}$, the condition (32) is required. In the case of $k_{\rm DD} \sim 1$, the condition (32) becomes Eq. (23). For the addressed spin with $\delta_n = 0$, we obtain

$$|\boldsymbol{a}_n^{(\pm)}| = \sqrt{\frac{2}{3}(2 \mp \sqrt{3})} |\boldsymbol{A}_n^x|. \tag{34}$$

For the resonance $k_{\rm DD}\omega_{\rm DD} = \nu_n$ we have the effective Hamiltonian

$$H_{\rm int}(t) \approx \frac{m_s}{4} f_{k_{\rm DD}} \sigma_z (\boldsymbol{A}_n^z - \boldsymbol{A}_n^z \cdot \hat{\nu}_n \hat{\nu}_n) \cdot \boldsymbol{I}_n, \tag{35}$$

when the oscillating terms can be neglected. The Hamiltonians Eq. (22) and Eq. (35) allow for the selective detection of individual nuclear spins in the ensemble. In the next section we will show that by means of an additional rf-field it also becomes possible to position these nuclear spins.

4. *Individual control of nuclear spins*

We can selectively control nuclear spins by rf control to allow for the positioning of the nuclear spin. To this end we apply the rf control field $H'_{\rm rfc}(t) = \sum_j \gamma_j V_{\rm rfc} \cos(\omega_{\rm rfc} t - \phi_{\rm rfc}) \hat{n}_{\rm rf} \cdot \boldsymbol{I}_j$. Similar to the derivation of Eqs. (13) to (17), in the rotating frame of $H_{\rm n}(t)$ the control field becomes

$$H_{\rm rfc}(t) = \sum_j \gamma_j V_{\rm rfc} \cos(\omega_{\rm rfc} t - \phi_{\rm rfc}) \tilde{\boldsymbol{n}}_j(t) \cdot \boldsymbol{I}_j, \tag{36}$$

where

$$\tilde{\boldsymbol{n}}_j(t) = \tilde{\boldsymbol{n}}_j^x \cos(\omega_{\rm rfd} t) + \tilde{\boldsymbol{n}}_j^y \sin(\omega_{\rm rfd} t) + \tilde{\boldsymbol{n}}_j^z(t), \tag{37}$$

$$\tilde{\boldsymbol{n}}_j^\alpha = (\boldsymbol{n}_j^\alpha - \boldsymbol{n}_j^\alpha \cdot \hat{\nu}_j \hat{\nu}_j) \cos(\nu_j t) - \hat{\nu}_j \times \boldsymbol{n}_j^\alpha \sin(\nu_j t) + \boldsymbol{n}_j^\alpha \cdot \hat{\nu}_j \hat{\nu}_j. \tag{38}$$

As in the case for obtaining $\tilde{\boldsymbol{A}}_j(t)$ from $\boldsymbol{A}_j$, the vector $\tilde{\boldsymbol{n}}_j(t)$ is generated by rotating $\hat{n}_{\rm rf}$ about the axis $\hat{\omega}_j$ by an angle $\omega_{\rm rfd} t$ followed by the second rotation around the axis $\hat{\nu}_j$ by an angle $\nu_j t$.

When the decoupling control $H_{\rm rfd}(t) = 0$, $\tilde{\boldsymbol{n}}_j(t) = \boldsymbol{n}_j^x \cos(\omega_j t) + \boldsymbol{n}_j^y \sin(\omega_j t) + \boldsymbol{n}_j^z$. If we choose $\omega_{\rm rfc} = \omega_n$, the rf control field

$$H_{\rm rfc}(t) \approx \frac{1}{2} \gamma_n V_{\rm rfc} \boldsymbol{n}_n(\phi_{\rm rfc}) \cdot \boldsymbol{I}_n, \tag{39}$$

assuming that the rf driving is not too strong, i.e., $\gamma_n V_{\rm rfc} \ll \omega_n$ and $\gamma_n V_{\rm rfc} \ll \omega_n - \omega_j$ [see Eq. (9) for the expression of $\boldsymbol{n}_n(\phi_{\rm rfc})$].

When the decoupling control $H_{\rm rfd}(t) \neq 0$, $\tilde{\boldsymbol{n}}_j(t)$ has components oscillating at the frequency ν_j or $\omega_{\rm rfd} \pm \nu_j$. We choose weak rf driving $\gamma_n V_{\rm rfc} \ll \sqrt{3}\Delta \ll \omega_{\rm rfd}$ and $\gamma_n V_{\rm rfc} \ll \omega_n - \omega_j$. When the rf frequency is tuned to $\omega_{\rm rfc} = \omega_{\rm rfd} \pm \nu_n = \omega_n + (1 \pm \sqrt{3})\Delta$, we have the effective single spin control

$$H_{\rm rfc}(t) \approx \frac{\gamma_n V_{\rm rfc}}{4} \boldsymbol{b}_n^{(\pm)} \cdot \boldsymbol{I}_n, \tag{40}$$

$$\boldsymbol{b}_n^{(\pm)} \equiv \boldsymbol{n}_n(\phi_{\rm rf}) - \boldsymbol{n}_n(\phi_{\rm rf}) \cdot \hat{\nu}_n \hat{\nu}_n \pm \hat{\nu}_n \times \boldsymbol{n}_n(\phi_{\rm rf} + \frac{\pi}{2}). \tag{41}$$

While choosing $\omega_{\rm rfc} = \nu_j$, we obtain

$$H_{\rm rfc}(t) \approx \frac{1}{2} \gamma_n V_{\rm rfc} \boldsymbol{b}_n^{(z)} \cdot \boldsymbol{I}_n, \tag{42}$$

$$\boldsymbol{b}_n^{(z)} = (\boldsymbol{n}_n^z - \boldsymbol{n}_n^z \cdot \hat{\nu}_n \hat{\nu}_n) \cos\phi_{\rm rfc} - \hat{\nu}_n \times \boldsymbol{n}_n^z \sin\phi_{\rm rfc}. \tag{43}$$

In the next section we show how with these abilities of selectivity and tunable control on individual nuclear spins we can measure the positions of individual nuclei with high precision.

III. THE PROTOCOL AT WORK: MEASUREMENT OF HYPERFINE INTERACTIONS AND NUCLEAR POSITIONING

Our protocol measures the hyperfine vectors $\boldsymbol{A}_j$ and derives the positions of nuclei by studying the response of the electron spin quantum coherence to changes of the available control parameters. In this section we detail the individual steps of the protocol and demonstrate its effectiveness by means of numerical examples for realistic parameter sets.

We initialize the NV electron spin in a coherent superposition state $|\psi_x\rangle \equiv \frac{1}{\sqrt{2}}(|m_s\rangle + |0\rangle)$ with $m_s = \pm 1$ by optical initialization followed by a $\pi/2$ pulse [1, 2]. For temperatures significantly exceeding the nuclear spin Zeeman energy ($<$ MHz$\sim \mu$K), the nuclear spin state is well approximated by $\rho_B \propto I_B$ where I_B is the identity operator. Hence the initial state is $\rho(0) \propto |\psi_x\rangle\langle\psi_x| \otimes I_B$. Following this initialization procedure, we apply DD sequences and the rf fields. The population in the state $|\psi_x\rangle$, given by $p_{|\psi_x\rangle}(t) = \mathrm{Tr}\,[\rho(t)|\psi_x\rangle\langle\psi_x|]$, changes when the NV electron spin interacts with the nuclei. We use $L_{0,m_s}(t) = 2p_{|\psi_x\rangle}(t) - 1$ to describe the signal. In terms of the states $|m_s\rangle$ and $|0\rangle$, the quantity $L_{0,m_s}(t)$ is the off-diagonal part of the reduced NV electron density matrix and represents the quantum coherence [7, 35].

A. 3D positioning for non-interacting spins

For spins such that their dipolar coupling $H_{\rm nn}$ is negligible, we can individually address them without applying the rf decoupling field in Eq. (8). To illustrate this situation we have performed simulations on a diamond sample containing 442 ^{13}C spins which have been randomly generated on lattice sites of the diamond structure according to an abundance of 0.5 %. The simulations are carried out by disjoint cluster expansion including dipolar interactions up to a group size of six ^{13}C [35] and checked with cluster correlation expansion method [36]. We demonstrate the measurement of the hyperfine fields $\boldsymbol{A}_j$ and hence the positions of non-interacting nuclear spins.

1. *Addressing a single spin for measurement*

To measure the hyperfine vectors $\boldsymbol{A}_j$, we individually address the nuclear spins. According to the theory presented in Sec. II B 3, we tune the frequency $k_{\rm DD}\omega_{\rm DD} = \omega_{\rm scan}$ by changing the DD pulse intervals. When $\omega_{\rm scan}$ matches the resonance frequency of single nuclei, i.e., $\omega_{\rm scan} = \omega_j$, the coupling Hamiltonian in Eq. (22) is achieved. This interaction entangles the NV electron and the addressed nuclei which induces a dip on the NV coherence L_{0,m_s}. When only the n-th spin is addressed, from Eq. (22), the coherence reads

$$L_{0,m_s}(t) = \cos\left(\frac{1}{4} f_{k_{\rm DD}} |\boldsymbol{A}_n^x| t\right). \tag{44}$$

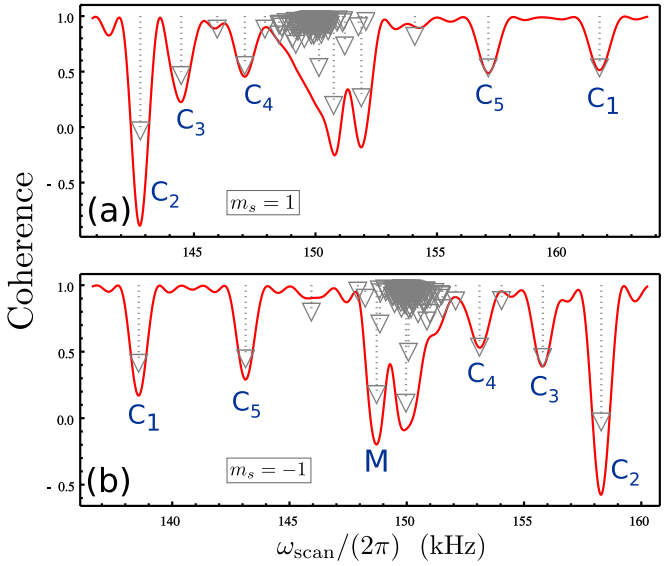

FIG. 2. (color online). Resonance patterns for a diamond sample containing 442 ^{13}C nuclei on randomly chosen lattice sites using the AXY sequences. The static magnetic field $B_z = 140.1$ G and the AXY sequences utilize the first harmonic ($k_{\rm DD} = 1$) and $f_1 = 0.06$. (a) and (b) corresponds to the choice of $m_s = +1$ or $m_s = -1$ NV state, respectively. The down arrows (with empty triangles as arrow heads) indicate the locations of ω_j, and the lengths of the arrows measure the relative coupling strengths $|\boldsymbol{A}_j^x|$. An addressed spin (the n-th spin) reduces the coherence by the factor given by Eq. (44), which appears as coherence dips on the spectra.

In Fig. 2, we apply a magnetic field $B_z = 140.1$ G (i.e., $\gamma_j B_z = 2\pi\times 150$ kHz for ^{13}C spins) along the NV axis, which is much stronger than the typical hyperfine fields $|\boldsymbol{A}_j|$ in the sample. To fulfill the conditions of Eqs. (23) and (24), we have used $k_{\rm DD} = 1$ and $f_1 = 0.02$ in the expansion, see Eq. (20). Here the AXY sequences have $f_k = 0$, k being 3 or any even number. To achieve a total evolution time of around 1 ms, 1520 pulses are used in the AXY sequences. (Note that, in total 304 robust composite X and Y pulses are applied given that each composite pulse consists of 5 elementary π pulses in the AXY sequences. Each DD period $2\pi/\omega_{\rm DD}$ contains two composite pulses while a minimal control circle in an AXY-8 sequence has 8 composite pulses.) By scanning the DD frequency $\omega_{\rm DD}$ for different values, clear coherence dips, which are signatures of spin addressing, appear, as shown in Fig. 2. These dips locate at the Larmor frequencies ω_j of the nuclear spins, as indicated by the down arrows on the figures. Each of the coherence dips marked by C$_j$ on the figures is caused by coupling to a single nuclear spin, which can be confirmed by the sinusoidal coherence oscillations when changing the total evolution time [6, 37]. However, the total DD sequence time has to be integer multiples of the DD pulse interval, which is synchronized with the resonant frequencies $\omega_j = k_{\rm DD}\omega_{\rm DD}$. Therefore, for a fixed magnetic field B_z, continuous plot of the coherence as a function of the total sequence time is impossible. We propose another way to confirm that the coherence dips C$_j$ are caused by coupling to a single nuclear spin.

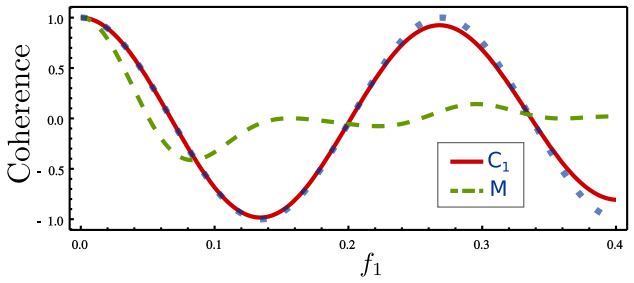

FIG. 3. (color online). Coherence oscillations as a function of f_1. Here f_1 by the AXY sequences can be tuned continuously and other parameters are the same as those in Fig. 2 (b). The red solid line shows the sinusoidal coherence oscillation when $\omega_{\rm scan}$ is set to the resonant frequency of the addressed spin denoted by C_1 in Fig. 2 (b), and the blue dots mark the curves calculated by Eq. (44). Green dashed line is the case that $\omega_{\rm scan}$ is set to the frequency dip denoted by M in Fig. 2 (b), where a few spins contribute the signal.

With the ability of modifying the f_1 coefficient by the AXY sequences, we can tune the NV-nucleus coupling strength continuously and linearly with f_1, and therefore obtain continuous change of the coherence as a function of f_1 (instead of total sequence time). The red solid line in Fig. 3 shows the coherence when we continuously change the value of f_1 while keeping other parameters unchanged and setting the frequency $\omega_{\rm scan}$ to the resonant frequency of a single nuclear spin. We can see clear sinusoidal coherence oscillation which fits the dynamics of a single spin. Note that there is a slight decay of the oscillation with increasing f_1, because a relatively large f_1 will violate the conditions Eqs. (23) and (24). This oscillation decay can be reduced by using a longer evolution time. For the coherence dip denoted by M in Fig. 2 (b), changing f_1 do not produce sinusoidal coherence oscillation, as shown by the green dashed line in Fig. 3, since the NV electron spin couples to more than one nuclear spins at the position M, at which we can see several resonant frequencies ω_j indicated in Fig. 2 (b). Without the ability of tuning f_k, e.g., by using CPMG or XY sequences, the coupling between NV electron and nuclear spins can not be tuned, and this limits the fidelity of two-qubit quantum gates since the interaction time has to be integer multiples of π/ω_j, which is fixed for the nuclear spins at a magnetic field. The oscillations of the coherence L_{0,m_s} tuned by f_1 demonstrate that we can finely change the interaction strength and hence enable high-fidelity two-qubit quantum gates between the NV electron and nuclei. For example, for the point with vanishing coherence L_{0,m_s} in Fig. 3 (a), the NV electron spin and the addressed spin are maximally entangled.

2. *Strength of hyperfine field*

After identifying the resonance frequencies ω_j by individual spin addressing, we can obtain the strengths of the hyperfine fields. The Larmor frequency ω_j =

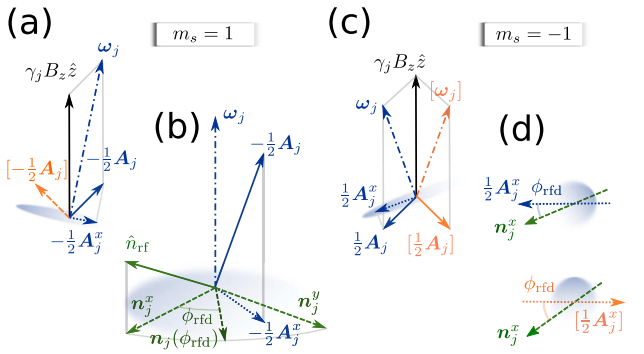

FIG. 4. (color online). Illustration of measuring the direction of $\boldsymbol{A}_j$ by using a rf control field to break the system symmetry. (a) and (b) sketch the vector relations with $m_s = 1$, while for (c) and (d) with $m_s = -1$. (a) and (b): the first scan of $\phi_{\rm rfc}$ (e.g., with using $m_s = 1$) left two possible directions of $\boldsymbol{A}_j$ using Eq. (45) [see (a) with the non-physical one denoted with "[]" in orange], because of the unknown sign in $\pm\boldsymbol{A}_j^x$ [see (b)]. (c) and (d): using another scan with different control parameters (e.g., changing m_s to $m_s = -1$), the physical solution of $\boldsymbol{A}_j$ is picked up. (c) shows the two possible ω_j for the two possible directions of $\boldsymbol{A}_j$ obtained from the first scan of $\phi_{\rm rfc}$. (d) shows that the angles between $\boldsymbol{n}_j^x$ and $\boldsymbol{A}_j^x$ are different when lying on the corresponding plane that is perpendicular to $\boldsymbol{\omega}_j$ or the non-physical one $[\boldsymbol{\omega}_j]$. Therefore, from the parallel condition Eq. (45) in the second scan with a different m_s from the one in the first scan, the actual direction of $\boldsymbol{A}_j^x$ is obtained. With the measured values of $A_j^{\parallel}$ and $A_j^{\perp}$, full information of $\boldsymbol{A}_j$ is measured.

$\sqrt{(\gamma_j B_z - \frac{m_s}{2}A_j^{\parallel})^2 + \frac{1}{4}(A_j^{\perp})^2}$ is a function of the parallel component $A_j^{\parallel} = \boldsymbol{A}_j \cdot \hat{z}$ of the hyperfine field along the $\hat{z}$ direction and the strength of perpendicular part $A_j^{\perp} = |\boldsymbol{A}_j - A_j^{\parallel}\hat{z}|$. Under a strong magnetic field we have $\omega_j \approx |\gamma_j B_z - \frac{m_s}{2}A_j^{\parallel}|$. In this way the coherence dips are approximately symmetric about $\gamma_j B_z$ under the transformation $m_s \to -m_s$ (although not exactly because of the direction and strength of $\boldsymbol{\omega}_j$ depend on m_s) see Figs. 2 (a) $m_s = 1$ and (b) $m_s = -1$. By measurements of ω_j using different NV states $|m_s\rangle$ or under different magnetic fields B_z, we obtain $A_j^{\parallel}$ and $A_j^{\perp}$ using the expression of ω_j. Note that we can also measure $|\boldsymbol{A}_n^x|$ by fitting the coherence data in Fig. 3 with Eq. (44). Under a strong magnetic field $|\boldsymbol{A}_n^x| \approx A_n^{\perp}$.

3. *Direction of hyperfine field*

The direction of $\boldsymbol{A}_j$ (note that $\boldsymbol{A}_j$ is a vectorial quantity) projected on the plane perpendicular to the magnetic field $B_z\hat{z}$ can not be inferred by only reconstructing ω_j, i.e. by measuring $A_j^{\parallel}$ and $A_j^{\perp}$. In this respect a method to estimate the relative directions of $\boldsymbol{A}_j$ has been recently proposed by utilizing nucleus-nucleus interactions [19] which, however, could be inaccurate because of weak dipolar coupling between the nuclei and the complicated dynamics of many-spin clusters.

Here, we show that the direction of $\boldsymbol{A}_j$ can be measured by

simply using the rf control field in Eq. (36). Note that both the effective field direction $\boldsymbol{n}_j(\phi_{\rm rfc})$ [see Eqs. (39) and (9)] and $\boldsymbol{A}_j^x$ in Eq. (22) lie in a plane perpendicular to $\hat{\omega}_j$, see Figs. 4 (a) and (b). The orientation of the vector $\boldsymbol{n}_j(\phi_{\rm rfc})$ in the plane orthogonal to $\hat{\omega}_j$ can be controlled by the phase $\phi_{\rm rfc}$. When $\boldsymbol{n}_j(\phi_{\rm rfc})$ and $\boldsymbol{A}_j^x$ are parallel, i.e.,

$$\boldsymbol{n}_j(\phi_{\rm rfc}) \times \boldsymbol{A}_j^x = 0, \tag{45}$$

the rf control Hamiltonian $H_{\rm rfc}(t)$ [see Eq. (39)] commutes with the interaction Hamiltonian $H_{\rm int}$ [see Eqs. (22) and (39) for the case without a rf decoupling field and Eqs. (28) and (40) when a rf decoupling field has been applied] and application of $H_{\rm rfc}(t)$ has no effect on the coherence of NV electron spin. Eq. (45) involves the values of the vectors $\hat{n}_{\rm rf}$ and $\boldsymbol{A}_j$, as well as the control parameters magnetic field strength B_z and magnetic number m_s. When $\boldsymbol{n}_j(\phi_{\rm rfc})$ and $\boldsymbol{A}_j^x$ are not parallel, the rf control field reduces the interaction between the NV electron and the addressed nuclear spin. This reduction of interaction is maximum when $\boldsymbol{n}_j(\phi_{\rm rfc})$ and $\boldsymbol{A}_j^x$ are perpendicular. Therefore, we can measure the solutions $\phi_{\rm rfc}$ to Eq. (45), by which we can infer the direction of $\boldsymbol{A}_j$ relative to the NV axis $\hat{z}$ and $\hat{n}_{\rm rf}$. An example of the coherence for a certain final evolution time as a function of phase $\phi_{\rm rf}$ is shown in Fig. 5, where vertical lines indicates the situation that $\boldsymbol{n}_j(\phi_{\rm rfc})$ and $\boldsymbol{A}_j^x$ are parallel. Eq. (45) is invariant under the transformation $\phi_{\rm rfc} \to \phi_{\rm rfc} + \pi$ (i.e., $\hat{n}_{\rm rf} \to -\hat{n}_{\rm rf}$), which implies that a single scan of $\phi_{\rm rfc}$ left two possible results $\pm\boldsymbol{A}_j^x$. Additionally we want to comment that the role of the rf field in our protocol is significantly different to the one in [20] where a rf $\pi/2$ pulse is used to complete the polarization transfer between the NV center and a target spin.

With two possible $\pm\boldsymbol{A}_j^x$, we obtain two possible hyperfine fields $\boldsymbol{A}_j$, see Fig. 4 (a) for the actual $\boldsymbol{A}_j$ and its non-physical mirror solution. The sign ambiguity of $\pm\boldsymbol{A}_j^x$ can be solved by noting that $\boldsymbol{A}_j$ and its non-physical mirror solution generally have different relative angles with respect to $\hat{n}_{\rm rf}$. For alignments that $\hat{n}_{\rm rf}$ is not perpendicular to the plane spanned by $\hat{z}$ and $\boldsymbol{A}_j^x$, as shown in Fig. 4, the angle between the projected vector $\boldsymbol{n}_j(0)$ and $\boldsymbol{A}_j^x$ [i.e., the solution $\phi_{\rm rfc}$ to Eq. (45)] changes when changing $\hat{\omega}_j$, which depends on the values of magnetic number m_s and magnetic field strength B_z.

4. *Measured positions*

Therefore, we can distinguish the signs of $\pm\boldsymbol{A}_j^x$ (hence the actual $\boldsymbol{A}_j$ and its non-physical mirror solution) by checking Eq. (45) for other parameters m_s and B_z. Here the changes of m_s already provide enough information to select the right sign of $\pm\boldsymbol{A}_j^x$. With the measured values of $A_j^{\parallel}$, $A_j^{\perp}$, and the direction of $\boldsymbol{A}_j^x$, the hyperfine field $\boldsymbol{A}_j$ is fully determined. Since the scheme does not rely on the amplitudes of the rf field $V_{\rm rfc}$, amplitude uncertainties do not affect the measurements.

The scheme measures the relative directions among $\hat{z}$, $\hat{n}_{\rm rf}$, and the hyperfine fields $\boldsymbol{A}_j$. If the direction of rf field $\hat{n}_{\rm rf}$ is unknown, we can define a coordinate system $\mathbb{S}$ by $\hat{z}$ and the

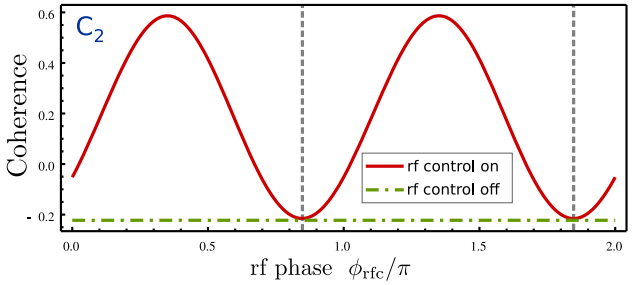

FIG. 5. (color online). Coherence L_{0,m_s} as a function of rf control phase $\phi_{\rm rfc}$. We set $\omega_{\rm scan}$ at the resonant frequency denoted by C_2 in Fig. 2 (a) and use $f_1 = 0.04$ for the AXY sequences. Other parameters are the same as those used in Fig. 2 (a). Red line is the coherence that a rf control field is applied with a driving amplitude $\gamma_j V_{\rm rfc} = 2\pi \times 1$ kHz for the ^{13}C spins. Green dashed dotted line is the coherence without rf control field ($V_{\rm rfc} = 0$). The vertical dashed lines denote the cases that $\boldsymbol{n}_j(\phi_{\rm rfc})$ and $\boldsymbol{A}_j^x$ are parallel.

hyperfine field $\boldsymbol{A}_j$ of one nuclear spin. In terms of $\mathbb{S}$, $\hat{n}_{\rm rf}$ is fixed and the hyperfine fields of other spins are measured in the coordinate $\mathbb{S}$. In our simulation, we assume unknown $\hat{n}_{\rm rf}$ and define the coordinate $\mathbb{S}$ that the hyperfine field $\boldsymbol{A}_j$ of the nucleus C_1 in Fig. 2 is aligned in the $x-z$ plane with $\boldsymbol{A}_j \cdot \hat{x} > 0$ (see Fig. 6 for the coordinate).

For nuclear spins not too close to the NV center (e.g., the case in our simulations), the hyperfine interaction $H_{\rm hf}$ takes the dipolar form and

$$\boldsymbol{A}_j = \frac{\mu_0}{4\pi}\frac{\gamma_e\gamma_j}{r_j^3}\left(\hat{z} - \frac{3\hat{z}\cdot\boldsymbol{r}_j\boldsymbol{r}_j}{|\boldsymbol{r}_j|^2}\right). \tag{46}$$

From the position dependence of $\boldsymbol{A}_j$, we obtain the nuclear positions $\boldsymbol{r}_j$ by solving Eq. (46). Note that the hyperfine interaction $H_{\rm hf}$ is symmetric under placing the nuclei at the opposite directions $\boldsymbol{r}_j \to -\boldsymbol{r}_j$. Therefore determining $H_{\rm hf}$ alone is not sufficient to distinguish the ambiguity of the sign in $\pm\boldsymbol{r}_j$. Using homogeneous magnetic fields along different directions cannot solve this ambiguity, since the Zeeman term $\gamma_j\boldsymbol{B}\cdot\boldsymbol{I}_j$ is invariant under $\boldsymbol{r}_j \to -\boldsymbol{r}_j$. However, we can solve this ambiguity by introducing a gradient magnetic field along the NV axis $B_z = B_z(\boldsymbol{r})$ to break the symmetry. When we know that the detected spins are placed at some regions, e.g., on top of the diamond surface (hence NV center), we do not need to distinguish $\pm\boldsymbol{r}_j$.

From the measured $\boldsymbol{A}_j$, we obtain the positions of the nuclear spins with distances r_j ranging from 0.92 to 1.38 nm. In Fig. 6, we show the actual positions (blue spheres) and the measured ones (red spheres) that are obtained by the measured hyperfine fields.

B. Individual 3D spin positioning for interacting spin clusters

In the previous subsection we have demonstrated the ability of our protocol to deliver positioning of nuclear spins with Angstrom precision in non-interacting spin clusters. In this

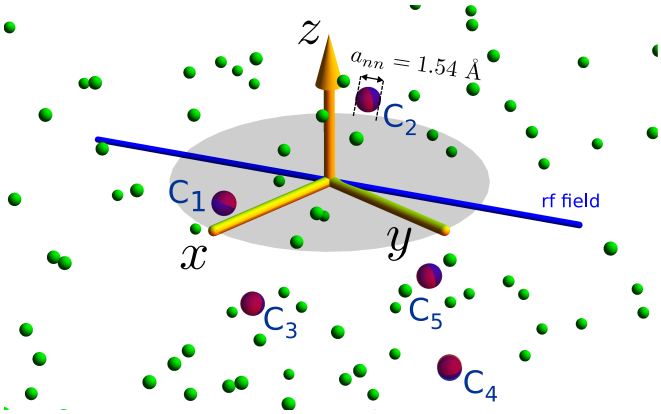

FIG. 6. (color online). Comparison of the measured (red spheres) and actual (blue spheres) ^{13}C positions, indicated by spheres of the diameter $a_{nn} = 1.54$Å that is the nearest neighbour distance of carbon atoms on the diamond lattice. Measurement uncertainties smaller than $0.5a_{nn}$ can already fix the positions of ^{13}C in the lattice sites of diamond. Their measured distances r_j rang from 0.92 to 1.38 nm. Other green spheres of a smaller size are other ^{13}C spins forming a spin bath. The shaded disk has a radius of 1 nm. The measured spin denoted by C_1 defines the coordinate which makes the C_1 spin lie in the $x-z$ plane. The blue line indicates the measured rf field direction $\pm\hat{n}_{\rm rf}$, which is almost parallel (indistinguishable) to the actual one.

subsection we are now turning to the case of interacting nuclear spin clusters. The procedure to measure the hyperfine fields $\boldsymbol{A}_j$ and therefore the positions of the nuclear spins is quite similar to that described in the previous subsection III A.

To show the working principles of our method in this case, we consider a cluster of three coupled nuclear spins (see Table I) of which the internuclear distances are a_{nn}, a_{nn}, and $2\sqrt{2/3}a_{nn}$. Here $a_{nn} = 1.54$ Å is the nearest neighbor distance between carbon nuclei in the diamond lattice. With a suitably tuned rf decoupling field we can suppress the internuclear dipolar coupling (see [25] and Sec. II B 1) and therefore enable individual spin addressing and positioning. We use a rf decoupling field with $\Delta = 20$ kHz to suppress internuclear dipolar coupling. This gives rise to the application of an rf field such that its Rabi frequency is $\approx \sqrt{2}\Delta$ which implies a decoupling field intensity of ≈ 28 G. Note that control fields with intensities around 0.1 T have already been implemented [38, 39]. In addition, unlike traditional nuclear magnetic resonance in solids that requires switching off of rf control fields to allow for detection windows, a stable rf decoupling field can be turned on during the whole period of our protocol, including NV electron spin initialization and readout, because the frequency of rf decoupling field is far off-resonance to the transition frequencies of the NV electron spin. Therefore, fast switching of rf decoupling is not required in our protocol, and we can use external coils that can avoid possible heating on the diamond sample. The Larmor frequency ω_j should be much larger than Δ to make the rf decoupling control possible. Thus we choose a strong magnetic field with $\gamma_j B_z = 900$ kHz for ^{13}C spins. To achieve a total evolution time of around 1 ms, the third harmonic ($k_{\rm DD} = 3$)

TABLE I. Nuclear positions in an interacting ^{13}C spin cluster as well as their measured values. The direction [1,1,1] is chosen as the NV symmetry axis and the NV center is located at [0,0,0].

	Nuclear positions (Å)	Measured values (Å)
Q_1	[3.57, 10.71, 3.57]	[3.56, 10.69, 3.55]
Q_2	[4.46, 9.82, 4.46]	[4.32, 9.82, 4.46]
Q_3	[3.57, 8.93, 5.36]	[3.65, 8.96, 5.23]

and 3040 pulses (i.e., 608 composite pulses) are used for the AXY sequences with $f_3 = 0.06$.

In Fig. 7 (a), we plot the coherence (red line) using the method that we have described in the previous subsection, i.e., without the application of rf decoupling field, which deviates considerably from the blue dashed line which is obtained by neglecting the internuclear interactions $H_{\rm nn}$. Indeed, a comparison with the blue dashed line shows that from the red coherence profile positioning of the nuclear spins in the spin cluster is not possible without the assistance of further numerical efforts invested to decode the spectrum. Although computationally feasible for the present case, such a numerical decoding rapidly becomes computationally challenging for even a moderate number of spins (see for example the case of malic acid studied in Section III C) especially when compared with the analysis of the signal provided by our method that can be effectively considered as generated from a set of non-interacting nuclear spins [see Fig. 7 (b)].

To demonstrate individual addressing and positioning of nuclear spins while suppressing $H_{\rm nn}$, we choose the control frequencies Eqs. (26) and (27). When $\omega_{\rm scan} = \omega_j$, we address the j-th nuclear spin with the interaction Hamiltonian Eq. (28). With the help of decoupling, we obtain clear single coherence dips as shown in Fig. 7 (b). The peaks caused by single spins Q_j are indicated. A comparison of Figs. 7 (a) and (b) reveals a small peak shift of order $\frac{1}{4}\frac{(\Omega_j^{\rm rfd})^2}{\omega_{\rm rfd}} \approx \frac{\Delta^2}{2\gamma_j B_z} \approx 0.22$ kHz which is analogous to the Bloch-Siegert shift [40] and originates from condition of Eq. (30). It should be stressed that this shift does not affect the single spin addressing capability. Indeed Fig. 7 (b) shows that in presence of the decoupling field, the signal response with and without internuclear interaction are essentially indistinguishable.

Because of the large magnetic field in this case, $\omega_j \approx |\gamma_j B_z - \frac{m_s}{2}A_j^{\parallel}|$ and we can write $\boldsymbol{A}_j \approx A_j^{\parallel}\hat{z} + A_j^{\perp}\hat{\theta}_j$, where the unit vector $\hat{\theta}_j$ is perpendicular to $\hat{z}$. We can obtain $A_j^{\parallel}$ with high accuracy using only the spectrum shown Fig. 7 (b). Under a rf decoupling field, the Hamiltonian addressing the j-th spin is described by Eq. (28) and it changes the coherence as

$$L_{0,m_s}(t) = L^j_{0,m_s}(t) \equiv \cos\left(\frac{1}{8}f_{k_{\rm DD}}|\boldsymbol{a}_j^{\pm}|t\right), \tag{47}$$

where the coupling strength $|\boldsymbol{a}_j^{(\pm)}|$ is proportional to $|\boldsymbol{A}_j^x| \approx A_j^{\perp}$ [see Eq. (34)]. Eq. (47) enables measurements of $A_j^{\perp}$.

We then apply a rf control field and obtain two possible horizontal directions $\pm\hat{\theta}_j$ by solving Eq. (45). From Fig. 7

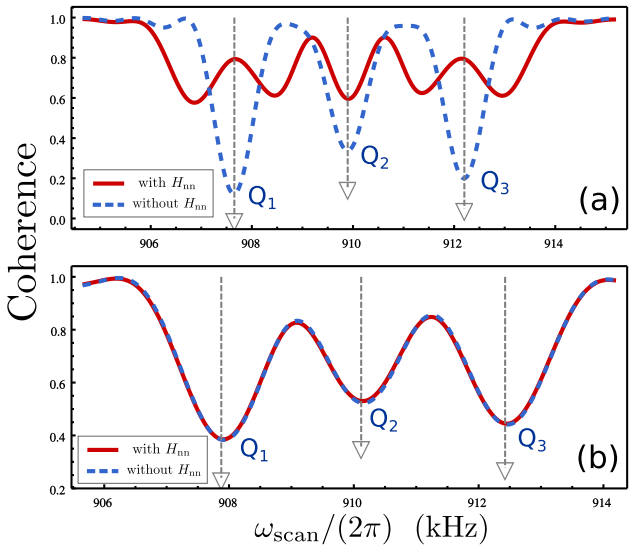

FIG. 7. (color online). Resonance patterns for a coupled cluster consisting of three ^{13}C spins in diamond shown in Table I). The magnetic field $B_z \approx 840.7$ G is applied along the NV symmetry axis and we choose $m_s = -1$. The vertical down arrows indicate the locations of single spin resonant frequencies, while their lengths denote the relative coupling strengths. The red solid line in (a) is the case without rf decoupling field, while the red line in (b) is the case that a rf decoupling field with $\Delta = 2\pi \times 20$ kHz is applied to suppress nuclear dipolar coupling. The blue dashed lines in (a) and (b) are the corresponding simulations without considering nuclear dipolar interaction. The application of rf decoupling reduces the electron-nuclear interactions by a factor $1/\sqrt{3}$ and hence reduces the separation between resonances.

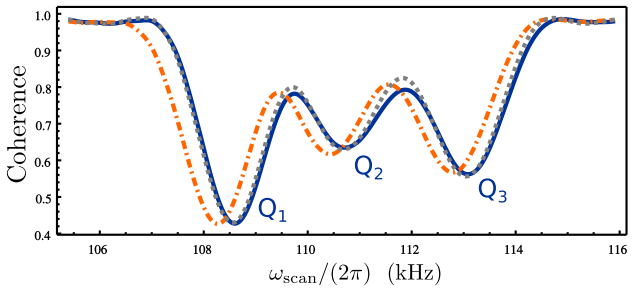

FIG. 8. (color online). Coherence signal of NV electron spin (the gray dotted line) modulated by the spin cluster denoted in Fig. 7 and the calculated ones using the measured parameters. The coherence calculated by the right choice of the measured parameters (the blue solid line) reproduces the actual one (the gray dotted line). Changing the measured values $\hat{\theta}_j$ to $-\hat{\theta}_j$ gives a calculated coherence (the orange dashed dotted line) that is different from the actual one. By comparing the actual coherence and the calculated ones, the directions of the hyperfine fields and hence the nuclear positions of the spin cluster are completely determined.

we know that the carbon atoms in the spin cluster are closely located. Without determining the sign of $\pm\hat{\theta}_j$, we find two possible positions of the spin cluster (the physical one with $\hat{\theta}_j$ and its rotated image with $\hat{\theta}_j \to -\hat{\theta}_j$). The measured results already provide complete information on the cluster structure (relative positions of nuclear spins). To distinguish the actual position relative to the NV center, we compare the calculated coherence signals with the actual one in Fig. 8, from which we rule out the non-physical one. The measured positions of the nuclear spins are listed in Table I, from which we can see that the errors are much smaller than the smallest distance between the carbon nuclei a_{nn} in the diamond lattice.

C. 3D imaging for bio-molecules

In this section we demonstrate that our method applies to the determination of the molecular structures. To this end we consider as an example of malic acid (molecular formula $C_4H_6O_5$) which plays an important role in biochemistry and is not too large to prevent exact numerical simulations. Malic acid has two stereoisomeric forms, L- and D-enantiomers. The L-malic acid is the naturally occurring form, while the structure of D-malic is the non-superimposable mirror reflection image of L-malic. Discriminating between the L and D-form typically requires macroscopic samples to allow for example the polarisation rotation of light. Here we aim to show that employing the methods that have been developed here it would become possible to achieve this task on the level of individual molecules. We perform the simulation for a molecule of L-malic acid placed on the surface of a diamond, and an NV center that is implanted 2 nm below the diamond surface. The molecule consists of four ^{12}C (natural abundance 98.89%), six ^{1}H (natural abundance 99.985%), and five ^{16}O (natural abundance 99.76%). The six ^{1}H spins in the molecule couple to the NV electron spin, and their locations are listed in Table II.

TABLE II. Positions of the ^{1}H spins in a molecule of L-malic acid used in the simulations, as well as the measured values. The direction [1,1,1] is chosen as the NV symmetry axis and the NV center is located at [0,0,0].

	Positions of ^{1}H spins (nm)	Measured values (nm)
H1	[1.5422, 1.2168, 0.4548]	[1.53, 1.24, 0.45]
H2	[1.7412, 1.3801, 0.6257]	[1.78, 1.33, 0.61]
H3	[1.5652, 1.4078, 0.6208]	[1.58, 1.40, 0.62]
H4	[1.8230, 1.2016, 0.4986]	[1.78, 1.29, 0.50]
H5	[1.4962, 1.1024, 0.7883]	[1.48, 1.14, 0.78]
H6	[1.7007, 1.6559, 0.4148]	[1.74, 1.61, 0.41]

We employ the methods described in the previous subsection III B to determine the nuclear positions. In the simulation, we apply a strong magnetic field $B_z \approx 1.057$ T. The AXY sequences utilize a high harmonic $k_{DD} = 225$ to reduce the total number of composite pulses to 1200, which corresponds to a total evolution time of around 3 ms. Compared with the case without rf decoupling in Fig. 9 (a), our method reveals the resonant structures [see Fig. 9 (b)] and enable individual measurements of the nuclear spins in the molecule. It can be seen in Fig. 9 that with the nuclear spins decoupled the signal of each spin resonance is more pronounced. The spins labeled by H2 and H4 are indistinguishable in the spectrum shown in

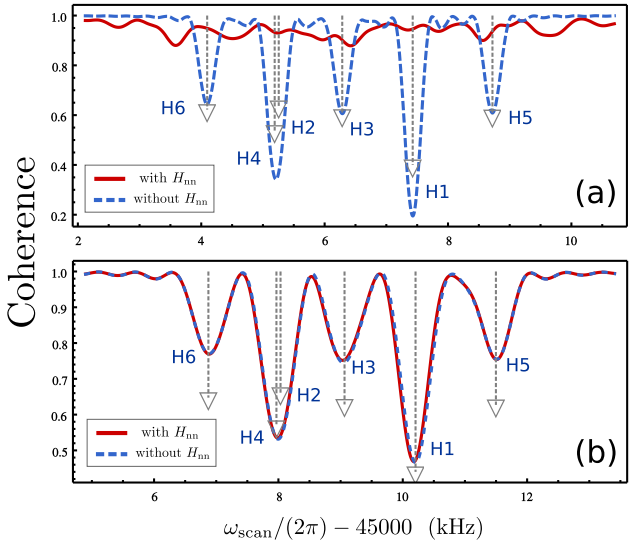

FIG. 9. (color online). Coherence signals between the NV $|-1\rangle$ and $|0\rangle$ states modulated by a L-malic acid molecule (see Table II for spin positions). A magnetic field $B_z \approx 1.057$ T is applied along the NV symmetry axis and we choose $f_{k_{\rm DD}} = 0.028$. The vertical down arrows indicate the locations of single spin resonant frequencies, with the lengths denote the relative coupling strengths. The red solid line in (a) is the case without rf decoupling field, while the red line in (b) is the case that a rf decoupling field with $\Delta = 2\pi \times 500$ kHz is applied to suppress nuclear dipolar coupling. The blue dashed lines in (a) and (b) are the corresponding simulations without considering nuclear dipolar interaction. The application of rf decoupling reduces the electron-nuclear interactions by a factor $1/\sqrt{3}$ and hence reduces the separation between resonances.

Fig. 9 (b). But since the spins are decoupled, we can identify from the coherence patterns at different control parameters that there are two addressed spins with approximately the same $A_j^{\parallel}$. Using a model of two nuclear spins, we obtain $A_j^{\perp}$ by fitting $\prod_{j=\rm H2,H4} L^j_{0,m_s}(t)$ [see Eq. (47)] with the coherence data and infer the directions by adding a rf control field. The measured positions of all the spins in the bio-molecule are listed in Table II. With the measured positions, we can identify that the malic acid is the L-enantiomer. With the resolved structure of the spins, the accuracy of the measured positions can be further improved if we compare the calculated and actual coherence data using a larger $f_{k_{\rm DD}}$ and (or) keeping nuclear dipolar coupling.

We can estimate the average time we need to resolve each individual peak in Fig. 9 as follows. Assuming a signal of ~ 0.1 (the signals in Fig. 9 (b) are larger), we need 100 measurements to reach the signal-to-noise threshold. Using a collection efficiency of 0.2 (see [19]), the time per shot equalling to the evolution time $\sim$ 3 ms (the time for NV initialization and measurement is a few microseconds and therefore negligible in the estimation), and a sampling of 10 points per peak, we find that a time of $\sim$ 15 seconds would be sufficient to resolve each peak. Similarly, the time to determine the relative direction of one spin is $\sim$ 15 seconds. In this manner, the extraction of each relative spin position takes ~ 0.5 minutes.

Finally, we want to comment that the noise induced by the surface proximity has been identified as a possible limiting factor for any method trying to obtain information about external spins. More specifically, in Ref. [41] that noise is determined as originating from two different sources, that is slow noise generated by a surface electronic spin bath and a faster noise attributed to surface-modified phononic coupling. In this respect we want to comment that while the slow frequency noise can be significantly mitigated by the application of a high number of microwave pulses, note that in our case the AXY sequence employs 1200 composite pulses, the faster noise can be reduced when the system is driven towards lower temperatures. Additionally we want to comment that further experimental developments as the one presented in Ref. [42] have significantly enhanced the coherence times of shallow NV centers. Furthermore, we want to remark that our method is equally useful for shorter DD sequences, i.e., when the sensing time of each run is reduced, and/or when applied on NV centers located at a larger distance from the surface. In these cases, the signal peaks have overlaps. However, the reconstruction of spin clusters can be efficiently assisted by numerical methods because of the presence of the decoupling field that allows to deal the measured signals as coming from non-interacting spins [7].

IV. SUMMARY AND DISCUSSIONS

We have developed methods to individually address and control interacting nuclear spins in ensembles through a single NV electron spin. Our protocol allows the suppression of unwanted nucleus-nucleus coupling and interactions between electron spin and the background noise. Thereby the hyperfine fields and hence the 3D positions of nuclear spins are measured. The interactions between the center electron spins and the addressed nuclear spins can be tuned continuously and are changeable to different types of interaction Hamiltonians. Therefore, high-fidelity two-qubit quantum gates between NV electron spin and nuclear spins or selective spin polarization can be implemented by our techniques. With the measurement of the nuclear positions of interacting spins, the structure of the spin clusters can be identified and the nuclear dipole-dipole interaction can be obtained. We applied the method to the measured the positions of all the proton spins in a molecule of L-malic acid to show the principles at work. The measured positions are sufficiently accurate to identify the stereoisomeric form of the molecule of malic acid. Our work paves the way to resolve and measure the structures of large-size nuclear spin clusters, which is ideal for solid-state quantum simulators with a long coherence time [25]. The theory and methods developed are not restricted to the study of nuclear spins and can be applied to other spin systems, e.g., systems of an NV center coupled to electron spin labels in bio-molecules.

ACKNOWLEDGEMENTS

This work was supported by the Alexander von Humboldt Foundation, the ERC Synergy grant BioQ, the EU projects DIADEMS, SIQS and EQUAM as well as the DFG via the SFB TRR/21 and the SPP 1601. Simulations were performed on the computational resource bwUniCluster funded by the Ministry of Science, Research and the Arts Baden-Württemberg and the Universities of the State of Baden-Württemberg, Germany, within the framework program bwHPC. We thank Fedor Jelezko and Thomas Unden for discussions.

Z.-Y. W. and J. C. contributed equally to this work.

Appendix A: Some details of the theory

1. Derivation for $\tilde{\boldsymbol{A}}_j(t)$

We calculate the field $\tilde{\boldsymbol{A}}_j(t)$ in Eq. (11) of the main text. $\tilde{\boldsymbol{A}}_j(t)\cdot\boldsymbol{I}_j = U_{\rm n}^{\dagger}(t)\boldsymbol{A}_j\cdot\boldsymbol{I}_j U_{\rm n}(t)$, where the unitary operator $U_{\rm n}(t) = \mathcal{T}e^{-i\int_0^t H_{\rm n}(\tau)d\tau}$ is governed by the Hamiltonian $H_{\rm n}(t) = H_{\rm nZ}^{\rm eff} + H_{\rm rfd}(t)$. We write $U_{\rm n}(t)$ in the rotating frame with respect to $H_{\rm nZ}^{\rm eff}$,

$$U_{\rm n}(t) = U_{\rm nZ}(t)\tilde{U}_{\rm rfd}(t), \tag{A1}$$

where $U_{\rm nZ}(t) = e^{-iH_{\rm nZ}^{\rm eff}t} = e^{i\sum_j \boldsymbol{\omega}_j\cdot\boldsymbol{I}_j t}$ and $\tilde{U}_{\rm rfd}(t) = \mathcal{T}e^{-i\int_0^t \tilde{H}_{\rm rfd}(\tau)d\tau}$ with $\tilde{H}_{\rm rfd}(t) = U_{nZ}^{\dagger}(t)H_{\rm rfd}(t)U_{nZ}(t)$. We obtain

$$\tilde{H}_{\rm rfd}(t) = \sum_j \gamma_j V_{\rm rfd}\cos(\omega_{\rm rfd}t-\phi_{\rm rfd})\tilde{\boldsymbol{n}}_j(t)\cdot\boldsymbol{I}_j, \tag{A2}$$

where

$$\tilde{\boldsymbol{n}}_j(t)\cdot\boldsymbol{I}_j = e^{-i\boldsymbol{\omega}_j\cdot\boldsymbol{I}_j t}\hat{n}_{\rm rf}\cdot\boldsymbol{I}_j e^{i\boldsymbol{\omega}_j\cdot\boldsymbol{I}_j t}. \tag{A3}$$

With the aid of the identity

$$e^{i\boldsymbol{I}_j\cdot\hat{l}\phi}\boldsymbol{I}_j\cdot\boldsymbol{b}e^{-i\boldsymbol{I}_j\cdot\hat{l}\phi} = \boldsymbol{I}_j\cdot[(\boldsymbol{b}-\boldsymbol{b}\cdot\hat{l}\hat{l})\cos\phi-\hat{l}\times\boldsymbol{b}\sin\phi+\boldsymbol{b}\cdot\hat{l}\hat{l}], \tag{A4}$$

which rotates the field $\boldsymbol{b}$ around the axis $\hat{l}$ by an angle ϕ, we get

$$\tilde{\boldsymbol{n}}_j(t) = \boldsymbol{n}_j^x\cos\omega_j t + \boldsymbol{n}_j^y\sin\omega_j t + \boldsymbol{n}_j^z, \tag{A5}$$
$$\boldsymbol{n}_j^x = \hat{n}_{\rm rf} - \hat{\omega}_j(\hat{n}_{\rm rf}\cdot\hat{\omega}_j), \tag{A6}$$
$$\boldsymbol{n}_j^y = \hat{\omega}_j\times\hat{n}_{\rm rf}, \tag{A7}$$
$$\boldsymbol{n}_j^z = \hat{n}_{\rm rf}\cdot\hat{\omega}_j\hat{\omega}_j. \tag{A8}$$

For the rf driving at the frequency $\omega_{rfd}\sim\omega_j\gg\gamma_j V_{\rm rfc}$, we apply the rotating wave approximation and get

$$\tilde{H}_{\rm rfd}(t) = \sum_j \frac{\gamma_j V_{\rm rfd}}{2}\left[\boldsymbol{n}_j^x\cos\varphi_j^{\rm rfd}(t) + \boldsymbol{n}_j^y\sin\varphi_j^{\rm rfd}(t)\right]\cdot\boldsymbol{I}_j, \tag{A9}$$

with $\varphi_j^{\rm rfd}(t) = \phi_{\rm rfd} - (\omega_{\rm rfd}-\omega_j)t$. The time dependence in $\tilde{H}_{\rm rfd}(t)$ can be removed in a frame $e^{i\sum_j(\omega_{\rm rfd}-\omega_j)\hat{\omega}_j\cdot\boldsymbol{I}_j t}$. That is,

$$\tilde{U}_{\rm rfd}(t) = e^{i\sum_j(\omega_{\rm rfd}-\omega_j)\hat{\omega}_j\cdot\boldsymbol{I}_j t}e^{-iH_\nu t}, \tag{A10}$$

where the Hamiltonian

$$H_\nu = \sum_j \boldsymbol{\nu}_j\cdot\boldsymbol{I}_j, \tag{A11}$$

$$\boldsymbol{\nu}_j = \frac{1}{2}\gamma_j V_{\rm rfd}\boldsymbol{n}_j(\phi_{\rm rfd}) + (\omega_{\rm rfd}-\omega_j)\hat{\omega}_j, \tag{A12}$$

with $\boldsymbol{\nu}_j$ given by Eq. (18). The magnitude of $\boldsymbol{\nu}_j \equiv \nu_j\hat{\nu}_j$ is $\nu_j = \sqrt{(\Omega_j^{\rm rfd})^2+(\omega_{\rm rfd}-\omega_j)^2}$, where the Rabi frequency on the nuclear spin $\Omega_j^{\rm rfd} = \frac{1}{2}\gamma_j V_{\rm rfd}|\boldsymbol{n}_j^{\phi_{\rm rfd}}|$ and $|\boldsymbol{n}_j^{\phi_{\rm rfd}}| = \sqrt{1-|\hat{n}_{\rm rf}\cdot\hat{\omega}_j|^2}$. Under a strong magnetic field $\hat{\omega}_j\approx\hat{z}$ and $|\boldsymbol{n}_j^{\phi_{\rm rfd}}|\approx\sqrt{1-|\hat{n}_{\rm rf}\cdot\hat{z}|^2}$. Summarizing Eqs. (A1) and (A10), we have, under the condition $\omega_{\rm rfd}\sim\omega_j\gg\gamma_j V_{\rm rfd}$,

$$U_{\rm n}(t) = U_\omega(t)U_\nu(t), \tag{A13}$$

where $U_{\omega,\nu}(t) = e^{-iH_{\omega,\nu}t}$ with

$$H_\omega = -\omega_{\rm rfd}\sum_j \hat{\omega}_j\cdot\boldsymbol{I}_j. \tag{A14}$$

Using Eqs. (A13) and (A4), we obtain Eq. (13) for the field $\tilde{\boldsymbol{A}}_j(t)$.

2. Decoupling of nucleus-nucleus interaction

The internuclear interaction is $H_{\rm nn} = \sum_{j>k}\frac{\mu_0}{4\pi}\frac{\gamma_j\gamma_k}{r_{j,k}^3}D_{(j,k)}$, where $r_{j,k}$ is the distance between the nuclear spins located at $\boldsymbol{r}_j$ and $\boldsymbol{r}_k$. The operator

$$D_{(j,k)} = \boldsymbol{I}_j\cdot\boldsymbol{I}_k - 3(\boldsymbol{I}_j\cdot\hat{r}_{j,k})(\hat{r}_{j,k}\cdot\boldsymbol{I}_k), \tag{A15}$$

where $\hat{r}_{j,k}$ is the unit vector of $\boldsymbol{r}_j-\boldsymbol{r}_k$. Here we show that, when dealing with the same nuclear specie ($\gamma_j\approx\gamma_k$), $H_{\rm nn}$ can be suppressed by the nuclear Hamiltonian $H_{\rm n}(t)$ even though the nuclear spins feel different Larmor frequency ω_j. Because $H_{\rm nn}$ is expressed by a linear combination of the operators $D_{(j,k)}$, it is sufficient to see the decoupling for two nuclear spins.

In the interaction picture of $H_{\rm n}(t)$, $\tilde{D}_{(j,k)}(t) = U_{\rm n}^{\dagger}(t)D_{(j,k)}U_{\rm n}(t) = U_\nu^{\dagger}(t)\tilde{D}_{(j,k)}^{(1)}(t)U_\nu(t)$, where $\tilde{D}_{(j,k)}^{(1)}(t) = U_\omega^{\dagger}(t)D_{(j,k)}U_\omega(t)$ is the operator written in the interaction picture of the Hamiltonian H_ω. For the Hamiltonian H_ω, each of the spins has an energy $\omega_{\rm rfd}$ much larger than the dipolar coupling. Therefore the terms in $D_{(j,k)}$ that do not conserve the energy carry fast oscillating factors in $\tilde{D}_{(j,k)}^{(1)}(t)$ and are suppressed by the large $\omega_{\rm rfd}$. Neglecting those terms that do not conserve the energy by the secular approximation (or equivalently by the rotating wave approximation), we have

$$\tilde{D}_{(j,k)}^{(1)}(t)\cong\frac{1}{2}[1-3(\hat{r}_{j,k}\cdot\hat{z})^2][3I_j^zI_k^z-\boldsymbol{I}_j\cdot\boldsymbol{I}_k], \tag{A16}$$

where $\cong$ means that the non-secular terms have been dropped out. That is, we have

$$H_{\rm nn}\approx\sum_{j>k}\frac{\mu_0}{8\pi}\frac{\gamma_j\gamma_k}{r_{j,k}^3}\left[1-3(\hat{r}_{j,k}\cdot\hat{z})^2\right]\left(3I_j^zI_k^z-\boldsymbol{I}_j\cdot\boldsymbol{I}_k\right). \tag{A17}$$

We consider the regime of strong magnetic field that $|\gamma_j B_z| \gg |\boldsymbol{A}_j|$. This allows the simplification that the unit vector $\hat{\omega}_j \approx \hat{z}$ and the Rabi frequency $\Omega_j^{\rm rfd} \approx \sqrt{2}\Delta$ are approximately the same. We define the coordinates $\hat{z} = \hat{\omega}_j$, $\hat{x} = \boldsymbol{n}_j(\phi_{\rm rfd})/|\boldsymbol{n}_j(\phi_{\rm rfc})|$, and $\hat{y} = \hat{z} \times \hat{x}$. In this coordinate, $\boldsymbol{\nu}_j = \sqrt{2}\Delta\hat{x} + (\Delta + \delta_j)\hat{z}$ with δ_j given by Eq. (10). If $\delta_j = 0$ the coupling operator $\tilde{D}^{(1)}_{(j,k)}(t)$ in Eq. (A16) can be further suppressed by the magic spinning. Here we show how to suppress the dipolar coupling in the realistic case that $\delta_j \neq 0$. Let a new coordinate $\hat{z}_j = \hat{\nu}_j$, $\hat{y}_j = \hat{y}$, and $\hat{x}_j = \hat{y}_j \times \hat{z}_j$, and define $I_j^{\alpha_j} = \boldsymbol{I}_j \cdot \hat{\alpha}_j$. We chose the detuning on the target coupled nuclei and driving amplitude that $\delta_j/\Delta \ll 1$ and define $\eta = (\delta_j + \delta_k)/\Delta$. We obtain

$$
\begin{aligned}
2I_j^z I_k^z &\cong \frac{2}{3} I_j^{z_j} I_k^{z_k}(1 + \frac{2}{3}\eta) + \frac{4}{3} I_j^{x_j} I_k^{x_k}(1 - \frac{1}{3}\eta) + O(\eta^2),\\
I_j^x I_k^x &\cong \frac{2}{3} I_j^{z_j} I_k^{z_k}(1 - \frac{1}{3}\eta) + \frac{1}{3} I_j^{x_j} I_k^{x_k}(1 + \frac{2}{3}\eta) + O(\eta^2),\\
I_j^y I_k^y &\cong I_j^{y_j} I_k^{y_k},
\end{aligned}
$$

which implies from Eq. (A16) that after rf decoupling $\tilde{D}^{(1)}_{(j,k)}(t) \cong O(\eta)$ has residual nuclear coupling because of $\delta_j \neq 0$. The residual coupling is suppressed by the reduction factor η. For the addressing of the k-th spin, we choose $\delta_k = 0$ and nuclear dipolar coupling to the addressed spin is negligible as long as the reduction factor $\eta = \delta_j/\Delta \ll 1$.

* zhenyu3cn@gmail.com
† jan.haase@uni-ulm.de
‡ jcasanovamar@gmail.com
§ martin.plenio@uni-ulm.de

[1] M. W. Doherty, N. B. Manson, P. Delaney, F. Jelezko, J. Wrachtrup, and L. C. L. Hollenberg, "The nitrogen-vacancy colour centre in diamond," Phys. Rep. **528**, 1 (2013).

[2] V. V. Dobrovitski, G. D. Fuchs, A. L. Falk, C. Santori, and D. D. Awschalom, "Quantum control over single spins in diamond," Annu. Rev. Condens. Matter Phys. **4**, 23 (2013).

[3] Y. Wu, F. Jelezko, M. B. Plenio, and T. Weil, "Diamond quantum devices in biology," Submitted to Angew. Chemie (2015).

[4] N. Zhao, J.-L. Hu, S.-W. Ho, J. T. K. Wan, and R.-B. Liu, "Atomic-scale magnetometry of distant nuclear spin clusters via nitrogen-vacancy spin in diamond," Nat. Nanotechnol. **6**, 242 (2011).

[5] S. Kolkowitz, Q. P. Unterreithmeier, S. D. Bennett, and M. D. Lukin, "Sensing distant nuclear spins with a single electron spin," Phys. Rev. Lett. **109**, 137601 (2012).

[6] T. H. Taminiau, J. J. T. Wagenaar, T. van der Sar, F. Jelezko, V. V. Dobrovitski, and R. Hanson, "Detection and control of individual nuclear spins using a weakly coupled electron spin," Phys. Rev. Lett. **109**, 137602 (2012).

[7] N. Zhao, J. Honert, B. Schmid, M. Klas, J. Isoya, M. Markham, D. Twitchen, F. Jelezko, R.-B. Liu, H. Fedder, and J. Wrachtrup, "Sensing single remote nuclear spins," Nat. Nanotechnol. **7**, 657 (2012).

[8] P. London, J. Scheuer, J.-M. Cai, I. Schwarz, A. Retzker, M. B. Plenio, M. Katagiri, T. Teraji, S. Koizumi, J. Isoya, R. Fischer, L. P. McGuinness, B. Naydenov, and F. Jelezko, "Detecting and polarizing nuclear spins with double resonance on a single electron spin," Phys. Rev. Lett. **111**, 067601 (2013).

[9] F. Shi, X. Kong, P. Wang, F. Kong, N. Zhao, R.-B. Liu, and J. Du, "Sensing and atomic-scale structure analysis of single nuclear-spin clusters in diamond," Nat. Phys. **10**, 21 (2014).

[10] V. V. Mkhitaryan, F. Jelezko, and V. V. Dobrovitski, "Highly selective detection of individual nuclear spins with rotary echo on an electron spin probe," Sci. Rep. **5** (2015).

[11] J. Casanova, Z.-Y. Wang, J. F. Haase, and M. B. Plenio, "Robust dynamical decoupling sequences for individual-nuclear-spin addressing," Phys. Rev. A **92**, 042304 (2015).

[12] T. van der Sar, Z. H. Wang, M. S. Blok, H. Bernien, T. H. Taminiau, D. M. Toyli, D. A. Lidar, D. D. Awschalom, R. Hanson, and V. V. Dobrovitski, "Decoherence-protected quantum gates for a hybrid solid-state spin register," Nature **484**, 82 (2012).

[13] T. H. Taminiau, J. Cramer, T. van der Sar, V. V. Dobrovitski, and R. Hanson, "Universal control and error correction in multi-qubit spin registers in diamond," Nat. Nanotechnol. **9**, 171 (2014).

[14] G.-Q. Liu, H. C. Po, J. Du, R.-B. Liu, and X.-Y. Pan, "Noise-resilient quantum evolution steered by dynamical decoupling," Nat. Commun. **4**, 2254 (2013).

[15] W. Pfaff, B. J. Hensen, H. Bernien, S. B. van Dam, M. S. Blok, T. H. Taminiau, M. J. Tiggelman, R. N. Schouten, M. Markham, D. J. Twitchen, and R. Hanson, "Unconditional quantum teleportation between distant solid-state quantum bits," Science **345**, 532 (2014).

[16] C. Müller, X. Kong, J. Cai, K. Melentijević, A. Stacey, M. Markham, D. Twitchen, J. Isoya, S. Pezzagna, J. Meijer, J. F. Du, M. B. Plenio, B. Naydenov, L. P. McGuinness, and F. Jelezko, "Nuclear magnetic resonance spectroscopy with single spin sensitivity," Nat. Commun. **5**, 4703 (2014).

[17] J. Cai, F. Jelezko, M. B. Plenio, and A. Retzker, "Diamond-based single-molecule magnetic resonance spectroscopy," New J. Phys. **15**, 013020 (2013).

[18] M. Kost, J. Cai, and M. B. Plenio, "Resolving single molecule structures with nitrogen-vacancy centers in diamond," Sci. Rep. **5**, 11007 (2015).

[19] A. Ajoy, U. Bissbort, M. D. Lukin, R. L. Walsworth, and P. Cappellaro, "Atomic-scale nuclear spin imaging using quantum-assisted sensors in diamond," Phys. Rev. X **5**, 011001 (2015).

[20] A. Laraoui, D. Pagliero, and C. A. Meriles, "Imaging nuclear spins weakly coupled to a probe paramagnetic center," Phys. Rev. B **91**, 205410 (2015).

[21] R. J. Epstein, F. M. Mendoza, Y. K. Kato, and D. D. Awschalom, "Anisotropic interactions of a single spin and dark-spin spectroscopy in diamond," Nat. Phys. **1**, 94 (2005).

[22] M. Lee and W. I. Goldburg, "Nuclear-magnetic-resonance line narrowing by a rotating rf field," Phys. Rev. **140**, A1261 (1965).

[23] A. Bielecki, A. C. Kolbert, and M. H. Levitt, "Frequency-switched pulse sequences: homonuclear decoupling and dilute spin NMR in solids," Chem. Phys. Lett. **155**, 341 (1989).

[24] E. Vinogradov, P. K. Madhu, and S. Vega, "Proton spectroscopy in solid state nuclear magnetic resonance with windowed phase modulated Lee-Goldburg decoupling sequences," Chem. Phys. Lett. **354**, 193 (2002).

[25] J. Cai, A. Retzker, F. Jelezko, and M. B. Plenio, "A large-scale quantum simulator on a diamond surface at room temperature," Nat. Phys. **9**, 168 (2013).

[26] Z.-Y. Wang, J. Cai, A. Retzker, and M. B. Plenio, "All-optical magnetic resonance of high spectral resolution using a nitrogen-vacancy spin in diamond," New J. Phys. **16**, 083033 (2014).

[27] W. Yang, Z.-Y. Wang, and R.-B. Liu, "Preserving qubit coherence by dynamical decoupling," Front. Phys. **6**, 2 (2011).

[28] H. Y. Carr and E. M. Purcell, "Effects of diffusion on free precession in nuclear magnetic resonance experiments," Phys. Rev. **94**, 630 (1954).

[29] S. Meiboom and D. Gill, "Modified spin-echo method for measuring nuclear relaxation times," Rev. Sci. Instrum. **29**, 688 (1958).

[30] A. A. Maudsley, "Modified Carr-Purcell-Meiboom-Gill sequence for NMR fourier imaging applications," J. Magn. Reson. (1969) **69**, 488 (1986).

[31] T. Gullion, D. B. Baker, and M. S. Conradi, "New, compensated Carr-Purcell sequences," J. Magn. Reson. (1969) **89**, 479 (1990).

[32] N. Zhao, J. Wrachtrup, and R.-B. Liu, "Dynamical decoupling design for identifying weakly coupled nuclear spins in a bath," Phys. Rev. A **90**, 032319 (2014).

[33] A. Albrecht and M. B. Plenio, "Filter design for hybrid spin gates," Phys. Rev. A **92**, 022340 (2015).

[34] W. Ma, F. Shi, K. Xu, P. Wang, X. Xu, X. Rong, C. Ju, C.-K. Duan, N. Zhao, and J. Du, "Resolving remote nuclear spins in a noisy bath by dynamical decoupling design," Phys. Rev. A **92**, 033418 (2015).

[35] J. R. Maze, J. M. Taylor, and M. D. Lukin, "Electron spin decoherence of single nitrogen-vacancy defects in diamond," Phys. Rev. B **78**, 094303 (2008).

[36] W. Yang and R.-B. Liu, "Quantum many-body theory of qubit decoherence in a finite-size spin bath," Phys. Rev. B **78**, 085315 (2008).

[37] M. Loretz, J. M. Boss, T. Rosskopf, H. J. Mamin, D. Rugar, and C. L. Degen, "Spurious harmonic response of multipulse quantum sensing sequences," Phys. Rev. X **5**, 021009 (2015).

[38] C. A. Michal, S. P. Hastings, and L. H. Lee, "Two-photon Lee-Goldburg nuclear magnetic resonance: Simultaneous homonuclear decoupling and signal acquisition," J. Chem. Phys. **128**, 052301 (2008).

[39] G. D. Fuchs, V. V. Dobrovitski, D. M. Toyli, F. J. Heremans, and D. D. Awschalom, "Gigahertz dynamics of a strongly driven single quantum spin," Science **326**, 1520 (2009).

[40] A. Abragam, *The principles of nuclear magnetism*, 32 (Oxford university press, 1961).

[41] Y. Romach, C. Müller, T. Unden, L. J. Rogers, T. Isoda, K. M. Itoh, M. Markham, A. Stacey, J. Meijer, S. Pezzagna, B. Naydenov, L. P. McGuinness, N. Bar-Gill, and F. Jelezko, "Spectroscopy of surface-induced noise using shallow spins in diamond," Phys. Rev. Lett. **114**, 017601 (2015).

[42] I. Lovchinsky, A. O. Sushkov, E. Urbach, N. P. de Leon, S. Choi, K. De Greve, R. Evans, R. Gertner, E. Bersin, C. Müller, L. McGuinness, F. Jelezko, R. L. Walsworth, H. Park, and M. D. Lukin, "Nuclear magnetic resonance detection and spectroscopy of single proteins using quantum logic," Science **351**, 836 (2016).